Nanoscale

PAPER

View Article Online
View Journal | View Issue

Cite this: *Nanoscale*, 2022, **14**, 11779

Oxidation of quantum dots encapsulated in block copolymer micelles as a function of polymer terminal charge†

Kil Ho Lee,[a] Brenton A. Noesges,[b] Chris McPherson,[b] Faiz Khan,[a] Leonard J. Brillson [b,c] and Jessica O. Winter [*a,d]

Most high-quality quantum dots (QDs) are synthesized in the organic phase, and are often coated with polymers for use in aqueous biological environments. QDs can exhibit fluorescence losses during phase transfer, but evaluating underlying mechanisms (*e.g.*, oxidation, surface etching, loss of colloidal stability) can be challenging because of variation in synthesis methods. Here, fluorescence stability of QDs encapsulated in block co-polymer (BCP) micelles was investigated as a function of BCP terminal functionalization (*i.e.*, –OH, –COOH, and $–NH_2$ groups) and synthesis method (*i.e.*, electrohydrodynamic emulsification-mediated selfassembly (EE-SA), sonication, and manual shaking). Fluorescence losses, fluorescence intensity, energy spectra, and surface composition were assessed using spectrofluorometry and cathodoluminescence spectroscopy (CL) with integrated X-ray photoemission spectroscopy (XPS). QDs passivated using charged BCPs exhibited 50–80% lower fluorescence intensity than those displaying neutral groups (*e.g.*, –OH), which CL/XPS revealed to result from oxidation of surface Cd to CdO. Fluorescence losses were higher for processes with slow formation speed, but minimized in the presence of poly(vinyl alcohol) (PVA) surfactant. These data suggest slower BCP aggregation kinetics rather than electrostatic chain repulsion facilitated QD oxidation. Thus, polymer coating method and BCP structure influence QD oxidation during phase transfer and should be selected to maximize fast aggregation kinetics.

Received 10th February 2022,
Accepted 11th July 2022

DOI: 10.1039/d2nr00778a

rsc.li/nanoscale

Introduction

Quantum dot (QD) semiconductor nanoparticles (NPs) display many useful properties for biological imaging, including size-tunable, narrow emission bandwidths, broad excitation spectra, and large optical cross sections.[1–4] These benefits are typically maximized by synthesis in the organic phase with subsequent transfer to an aqueous phase *via* ligand exchange[5] or encapsulation,[6] often using amphiphilic polymers.[7] However, despite reports of resistance to photobleaching,[8–17] transfer processes can induce fluorescence losses resulting from surface etching,[18,19] loss of colloidal stability,[20] or oxidation.[21] For example, reversible[18,22] or irreversible[19] defect states on the QD surface, known as quenching centers, can occur during ligand exchange transfer processes.[18,19,22,23] Additional defects can be introduced *via* surface oxidation,[24,25] which is accelerated in aqueous media,[20,22] and which may occur independently[25] or in concert with ligand loss.[22,26] Poor passivation resulting from loss of coordinating ligands can also lead to loss of colloidal stability, aggregation, and NP growth *via* Ostwald ripening processes,[27] all of which reduce fluorescence signal. Attempts to reduce fluorescence loss have focused on schemes that reduce surface etching by leaving the original ligands in place (*e.g.*, as micelle encapsulation[28,29]) that minimize oxidation by the use of thick polymer coatings[20] or that increase colloidal stability through charge-balanced zwitterionic coatings.[30]

Recently, we[31] and others[32] have reported co-encapsulation of multiple NPs in block co-polymer (BCP) micelles as a mean to provide multifunctionality (*e.g.*, superparamagnetic iron oxide NPs (SPIONs) for magnetism and QDs for imaging) or to increase overall particle properties (*e.g.*, 4–13 times increased fluorescence and reduced blinking through the combinatorial

[a]*William G. Lowrie Department of Chemical and Biomolecular Engineering, The Ohio State University, 151 W. Woodruff Ave., Columbus, OH 43210, USA. E-mail: winter.63@osu.edu*
[b]*Department of Physics, The Ohio State University, 191 W. Woodruff Ave., Columbus, OH 43210, USA*
[c]*Department of Electrical and Computer Engineering, The Ohio State University, 205 Dreese Lab, 2015 Neil Ave, Columbus, OH 43210, USA*
[d]*Department of Biomedical Engineering, The Ohio State University, 151 W. Woodruff Ave., Columbus, OH 43210, USA*
† Electronic supplementary information (ESI) available. See DOI: https://doi.org/10.1039/d2nr00778a

effect of multiple encapsulated QDs[29]). We have shown that this approach can reduce photo-oxidation[33] compared to thinner lipid–polymer[28] or intercalating polymer[7] coatings used in other aqueous QD solubilization schemes. However, current synthesis methods typically require large amounts of surfactant (>99% by weight) to promote self-assembly of the bulky BCPs employed. These surfactants are often viewed as benign, but have the potential to interact with BCPs, QDs, and ligands on the QD surface. For example, surfactants have been shown to induce ligand loss through a wrap-and-wrest mechanism that yields surface etching and reduced fluorescence.[19]

The use of large amounts of surfactant has also limited investigation of the influence of polymer functionalization, such as terminal functionalizations (*e.g.* –COOH) for bioconjugation,[34] on the QD surface. Although often viewed as interchangeable, BCPs with different functional groups experience different interchain charge repulsion and possess different aggregation rates (*e.g.*, synthesis kinetics), all of which could influence the compactness of the resultant micelle. As with the approach[33] where small molecules, or ions, are adsorbed to form compact surface monolayers that increase QD stability, ensuring the structural integrity and compact packing geometry of the polymer chains forming the micelle may be critical to preserving fluorescence by reducing NP exposure to the external environment. Given that several groups are currently pursuing BCP-based approaches for QD phase transfer,[29,35–38] increased understanding of the role of BCP termination on QD fluorescence properties could greatly enhance the utility of these composites for bio-imaging. Here, we evaluated QD fluorescence loss as a function of BCP amphiphile termination using model polystyrene-polyethylene oxide (PS-PEO) BCPs terminated with –OH, –COOH, or $-NH_2$ functional groups. These studies were enabled by our development of a novel, surfactant-free micelle synthesis process: electrohydrodynamic emulsification-mediated self-assembly (EE-SA).[39] This approach is based on our prior Aero-IS process,[38] but generates an emulsion by spray of non-conductive organic directly into the conductive aqueous phase, thereby eliminating the need for surfactant as a driving fluid. Composites were evaluated *via* a combination of advanced analysis techniques, including fluorescence spectroscopy, cathodoluminescence spectroscopy (CL), and X-ray photoelectron spectroscopy (XPS) to identify fluorescence losses and correlated changes in the QD electron band structure. The direct integration of CL and XPS enabled the mechanistic source of these changes to be identified.

Results

Nanocomposite formation and characterization

The electrospray emulsion (EE) technique enables surfactant free, oil-in-water self-assembly (SA) of BCP micelles encapsulating NPs,[39] including QD micelles (*i.e.*, MultiDots[29]). Here, we used this approach to encapsulate QDs in PS-PEO micelles terminated with –OH, –COOH, and $-NH_2$ functional groups and studied the effect of BCP termination on resulting composite fluorescence. Transmission electron microscope (TEM) images revealed different QD aggregation morphologies within MultiDot nanocomposites (Fig. 1). QDs encapsulated in –OH terminated BCPs were well distributed within micelles, whereas –COOH and $-NH_2$ terminated BCPs resulted in particle aggregates. This behaviour was particularly pronounced for –COOH MultiDots for which QDs appeared to form a tight aggregate bundle within micelle cores or located near micelle surfaces. MultiDots terminated with $-NH_2$ groups showed QD aggregates localized toward the micelle interior. Encapsulation efficiencies were similar for –OH and –COOH MultiDots (16.3 ± 1.3% *vs.* 14.5 ± 1.3%, respectively), but lower for $-NH_2$ terminated MultiDots (7.7 ± 0.4%). Encapsulation efficiency reflects losses both from unencapsulated QDs (not observed) and MultiDots lost during purification. MultiDot sizes were characterized using TEM analysis. Similar to our previous work,[39] nanocomposite MultiDots exhibited spherical micelle sizes of 53.8 ± 13.0 nm for –OH terminated BCPs and 72.0 ± 14.9 nm for –COOH terminated BCPs (Table 1). MultiDots synthesized from $-NH_2$ terminated polymers were difficult to characterize, most likely because of residual salts in the polymer solution, yielding a mix of spherical, elliptical, and wormlike, micelles.

Fluorescence stability of QDs in micelles: role of the BCP terminal group

In this study, the fluorescence intensity of QD-loaded micelles passivated using model PS-PEO BCPs with –OH, –COOH, and $-NH_2$ terminal functionalization was evaluated (Fig. 2). For each BCP functionalization, two types of QDs were examined: green (λ_{em} = 540 nm) and red CdSe/ZnS QDs (λ_{em} = 600 nm). These two were chosen because green QDs (diameter ~3 nm) are smaller and have a higher surface to volume ratio, thus would be expected to show increased susceptibility to surface chemistry effects relative to red QDs (diameter ~5nm). For both QD sizes, fluorescence intensity was significantly higher for micelles synthesized using –OH terminated BCPs than for –COOH or $-NH_2$ terminated BCPs. In addition, reduction of fluorescence signal for green QDs was higher than that of red QDs, consistent with losses related to surface damage. However, time-dependent fluorescence decay was not observed for any sample over the course of this study (*i.e.*, 7 days). In addition, no changes in the absorbance or fluorescence emission peaks compared to the organic unencapsulated QDs were observed (Fig. S1†).

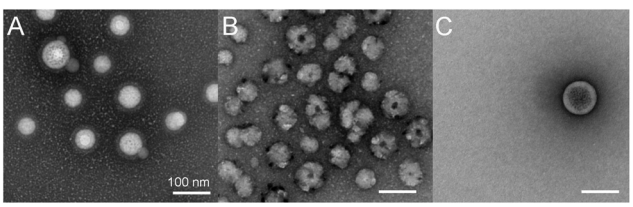

Fig. 1 Transmission electron microscope images of MultiDots, *e.g.*, QDs encapsulated in PS-PEO BCPs with (A) –OH, (B) –COOH, and (C) NH_2 terminations. Scale bar = 100 nm.

Table 1 TEM size analysis results for PS-PEO MultiDots terminated with –OH and –COOH groups at QD : PS-PEO ratio of ~0.005. $N > 200$. L_F = Feret length, % by N = the number percent, AR = the average aspect ratio

	Multidots terminated with –OH				Multidots terminated with –COOH		
	L_F (nm)	% by N	AR		L_F (nm)	% by N	AR
Sphere	53.8 ± 13.0	75	1.07 ± 0.07	Sphere	72.0 ± 14.9	77.3	1.13 ± 0.07
Ellipse	77.8 ± 15.0	24.1	1.55 ± 0.19	Ellipse	91.4 ± 20.0	17.9	1.57 ± 0.21
Worm	96.8 ± 3.2	0.9	2.12 ± 0.15	Worm	129.7 ± 24.4	4.8	2.41 ± 0.28

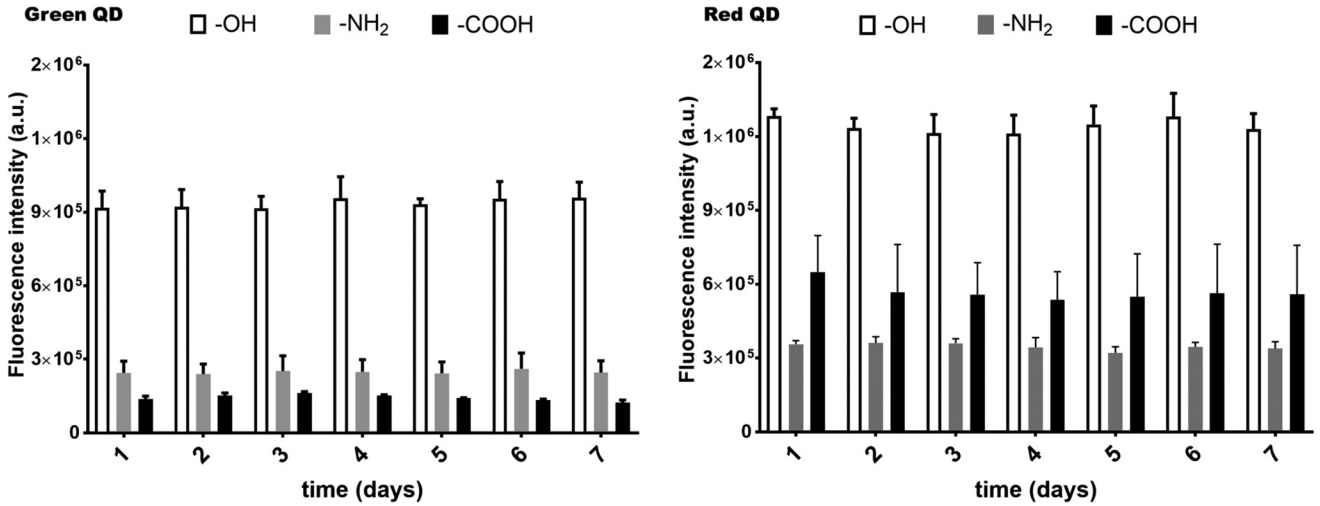

Fig. 2 Fluorescence intensity of QDs encapsulated in PS-PEO BCPs terminated with –OH, –COOH, and –NH_2. Day 1 is the day the nanocomposites were synthesized, following solvent evaporation.

To confirm these data, we also evaluated fluorescence quantum yield (QY) for red QD MultiDots (Fig. S2†). Similar to fluorescence intensity, –OH MultiDot QY was much higher than that of either charged BCP (16% for –OH *vs.* 5% for –NH_2 and ~1% for –COOH); all values remained relatively constant throughout the 7 days of analysis. However, –COOH QY values were lower than those of –NH_2, an inverse behaviour from their fluorescence intensity.

It is possible that these observations are simply the result of different QD encapsulation efficiencies for BCPs with different terminations. Reduced QY, but higher fluorescence intensity, of –COOH MultiDots *vs.* –NH_2 terminated MultiDots supports this theory. However, encapsulation efficiencies for –OH and –COOH terminated MultiDots were fairly similar, which does not support this theory. Alternatively, we[40] and others[20] have shown that micelle encapsulation affords better protection against photo- or chemical oxidation compared to ligand exchange or other polymer coating methods. Although not fully understood, the micelle chains may provide a diffusive barrier to oxidation. Thus, an alternative possibility is that BCPs with charged terminations reduce protection against oxidation.

QD energy spectra as a function of BCP terminal charge

To distinguish the effect of other QD surface defects from that of oxidation, cathodoluminescence spectroscopy (CL) with curve fitting and deconvolution was performed on CdSe/ZnS QDs encapsulated in BCPs with –OH, –COOH, and –NH_2 terminations (Fig. 3). The corresponding empty micelles were also evaluated as a control. The band gap of bulk CdSe at room temperature is 1.74 eV.[41] However, the band gap for QDs varies based particle size[42] and the thickness of the shell (*i.e.*, ZnS).[43] Further, polymer coating can also change QD band gap.[44] Thus, CL spectra of MultiDots were expected to include a CdSe band gap peak, an emission peak, and other peaks from ZnS and the polymer coating. In the CL scans for empty micelles (Fig. 3(A)–(C)), the dominant features occur at energies >3.0 eV. Previous studies report optical energy gaps (E_g) for PS and PEO ranging from 2 to 4 eV, depending on the presence of additives.[45,46] Thus, consistent with reports, these regions of the spectra were attributed to the polymer.

Deconvolution of CL scans for red QD-containing MultiDots (Fig. 3(D)–(F)) revealed a peak centered between 2.07–2.09 eV regardless of BCP termination, which was attributed to their expected emission signal (λ_{em} ~ 600 nm, 2.07 eV). Below this emission peak, a peak observed near 1.82–1.84 eV in each sample was attributed to the CdSe/ZnS QD band gap. Compared to empty micelle controls a new peak between 2.27–2.29 eV also emerged. This energy corresponds to the bandgap of cadmium oxide (CdO), potentially indicating QD oxidation.[47] Comparing –OH terminated BCP samples to

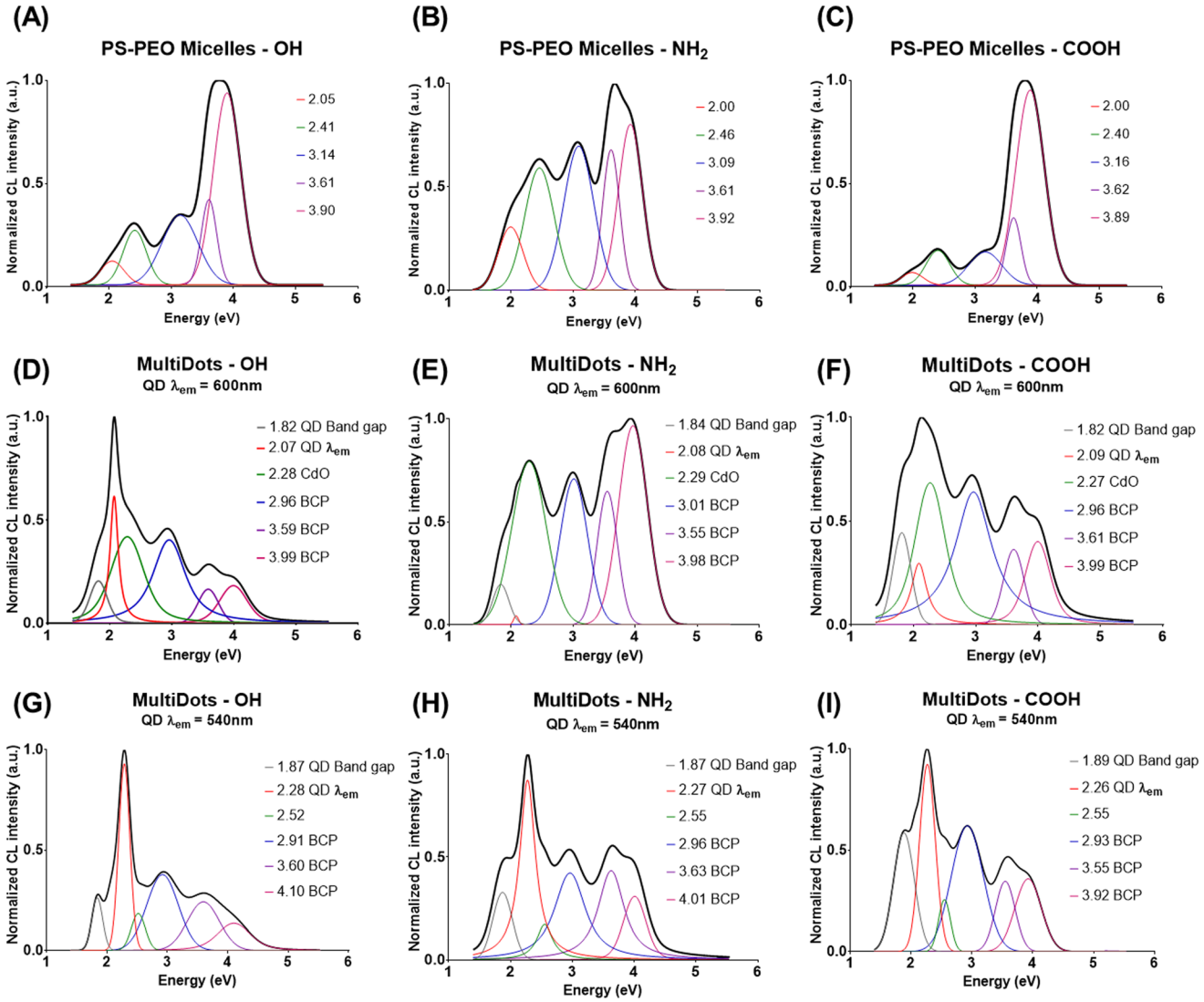

Fig. 3 CL spectroscopy of (A–C) empty micelles passivated from BCPs terminated with (A) –OH, (B) $-NH_2$, and (C) –COOH; (D–F) MultiDots encapsulating red QDs (λ_{em} = 600 nm) with 8 BCPs terminated with (D) –OH, (E) $-NH_2$, and (F) –COOH; (G–I) MultiDots encapsulating green QDs (λ_{em} = 540 nm) with BCPs terminated with (G) –OH, (H) $-NH_2$, and (I) –COOH.

–COOH and $-NH_2$ terminated BCP samples, the 2.27–2.29 eV peak intensity relative to the emission peak at 2.07–2.09 eV followed the trend NH_2 > COOH > OH. These results inversely correspond with luminescence data (Fig. 2), in which the greatest fluorescence signals were seen for –OH terminated BCPs. In CL scans of green QD-containing MultiDots (Fig. 3(G)–(I)), the expected QD emission peak (λ_{em} ~ 540 nm, 2.27 eV) and the bandgap of CdO (2.28 eV) could not be distinguished, so similar analysis could not be performed.

QD surface defect characterization

To confirm the identity of the defect peak at ~2.28 eV as CdO, X-ray photoelectron spectroscopy (XPS) was performed on empty micelles and MultiDots encapsulating red QDs using –OH and –COOH terminated BCPs. Because the polymer radius of gyration was larger than escape depth of the photoelectrons generated by XPS,[48,49] photoelectrons with binding energies characteristic of Se, Zn, or S associated with QDs were not clearly observed (Fig. S3†). Hence, we evaluated O 1s and Cd 3d core levels to measure the energy spacing between core levels and identify the presence of a metal oxide (Fig. 4). Photoelectron emission observed from Cd, but not Zn, Se, or S likely indicated that some Cd was released from the QDs during MultiDot formation. Further, angle resolved XPS (ARXPS) was used to investigate the distribution of Cd within the polymer as a function of depth.

The O 1s core level spectra (Fig. 4(A), (B) & (E)) contain two main components, a dominant peak near 532 eV and a lower binding energy side component near 532 eV. The dominant component at ~532 eV indicates C–O binding which was expected. The formation of metal oxide, as shown by the side peak at ~530 eV, was present at all angles in the –COOH BCP

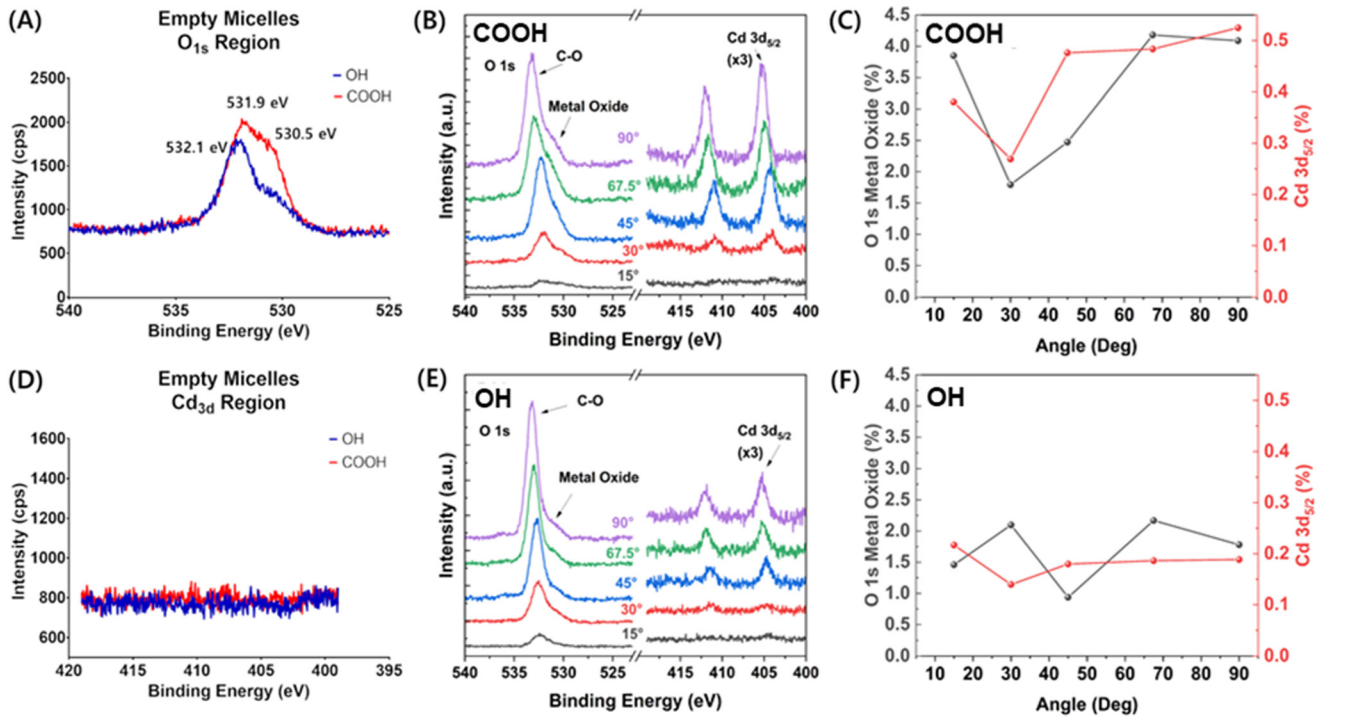

Fig. 4 (A) O 1s core level for empty micelles, (B) ARXPS data for –COOH MultiDots encapsulating red QD (λ_{em} = 600 nm), (C) relative concentration of Cd $3d_{5/2}$ core level and metal oxide O 1s component demonstrating correlated behavior for –COOH MultiDots, (D) Cd 3d core level spectra for empty micelles, (E) ARXPS data for –OH MultiDots encapsulating red QD (λ_{em} = 600 nm) and (F) relative concentration of Cd $3d_{5/2}$ core level and metal oxide O 1s component for –OH MultiDots demonstrating reduced concentration of both compared to –COOH MultiDot sample.

terminated MultiDot samples (Fig. 4(C)). Oxide peaks were greatly diminished in the –OH MultiDot samples (Fig. 4(F)), consistent with fluorescence and CL measurements. The O 1s spectra for both empty micelle samples show components around 530 eV (Fig. 4(A)) despite a lack of Cd 3d core level peak (Fig. 4(D)). Other features observable in the wide energy range survey scans suggest potential salt contamination of the polymers, (*i.e.*, sodium) which could explain the additional O 1s component observed in these samples (Fig. S4†). For MultiDots of either BCP termination, the Cd core level spectra (Fig. 4(B) & (E)) show peaks between 404–405 eV and 411–412 eV corresponding to the $3d_{5/2}$ and $3d_{3/2}$ spin–orbit split levels, respectively. The Cd 3d spin–orbit splitting for –COOH MultiDots was 6.76 eV and 6.75 eV for –OH MultiDots, both in good agreement with the expected splitting.[50] Since the C 1s core level spectra contains components related to both the BCP and adventitious carbon, a charge correction referencing the adventitious C 1s binding energy of 284.8 eV would be unreliable for assigning absolute binding energies. However, the energy difference between two core levels, *e.g.*, the metal oxide O 1s component at ~530 eV and Cd $3d_{5/2}$ at ~404 eV, is unaffected by charge corrections. The angle-resolved average binding energy separation for the –COOH MultiDot samples is 126.1 eV, whereas the energy separation was 126.0 eV for –OH MultiDots. This energy separation is in good agreement with CdO derived from $Cd(OH)_2$.[51] Additionally, in the –COOH MultiDots, the relative concentration of Cd is correlated with the relative amount of the metal oxide O 1s component (Fig. 4(C)) providing further evidence for CdO formation. The –OH MultiDot sample shows far less Cd (Fig. 4(F)) compared to the –COOH MultiDot sample (Fig. 4(C)) which is consistent with the diminished metal oxide O 1s feature, and CL and fluorescence measurement in the –OH MultiDots. These data support our hypothesis that the defect peak evidenced in CL at ~2.28 eV most likely belongs to CdO.

One possible explanation for increased surface oxidation for micelles formed using BCPs terminated with charged functional groups is that charge-induced repulsion of neighboring PEO chains diminished micelle stability or coating compactness. As suggested by the increased size of –COOH (and $–NH_2$) terminated micelles relative to –OH terminated micelles, electrostatic repulsion between neighboring BCP chains may lead to corona swelling. This swelling may, in turn, reduce structural integrity, thereby increasing the likelihood of defect-forming reactions at the QD surface. The degree of oxidation may depend on the presence of charged end-groups and the repulsion they introduce between neighboring chains, resulting in less compact micelles. Schematics often present functional groups as primarily residing on the micelle surface, and indeed our zeta potential measurements indicate the presence of respective charged *versus* neutral groups for micelles synthesized with each BCP termination (Fig. S5†) (*i.e.*, neutral for –OH, slightly positive for $–NH_2$, and negative for –COOH terminations). However, in practice only ~20% of groups would

likely be found on the micelle surface as a result of interfacial surface tension between the polymer blocks.[51] Thus, a large number of terminal groups would be available to influence the interior micelle structure. However, the fluorescence stability observed over time does not fully support this theory (Fig. 2), in which continual fluorescence losses would be expected. Fluorescence loss appears to occur during coating formation or at least within the first 24 hours following coating formation. Thus, an alternative possibility is the introduction of surface defects during nanocomposite formation.

QD energy spectra as a function of aqueous transfer method

To evaluate this hypothesis, we first synthesized composites using EE in the presence of a nitrogen blanket, but we did not observe any statistical differences in QY for –COOH or –NH_2 MultiDots synthesized *via* this approach *versus* in open air (Fig. S6†). Thus, air exposure alone does not account for the observed oxidation. We next examined composites synthesized using different approaches. Similar to Sun *et al.*,[52] MultiDots encapsulating red QDs were synthesized using the interfacial instability process (IS) (which utilizes large amounts of PVA surfactant) *via* manual shaking and probe sonication. Previously, we[37] and others[52] have observed that –OH MultiDots synthesized *via* IS-sonication[37] or manual shaking[52] display sizes of ~30–40 nm, smaller than what we observe here (Fig. 1). However, these composites incorporate large amounts of PVA, which influences their size. In this size range, each micelle incorporates only a few QDs.

BCPs terminated with –COOH were employed as a model system because of their reduced fluorescence (Fig. 2). For samples synthesized *via* manual shaking, weak QD aggregates stabilized with PVA were separated from MultiDots and analyzed alongside soluble MultiDot samples (Fig. S7†). Although they precipitated from solution, these QD-PVA aggregates were highly fluorescent, whereas the MultiDots fraction of manual shaking solutions showed weak fluorescence. MultiDots synthesized *via* sonication were also fluorescent, but with lower intensity than PVA aggregates created *via* manual shaking. QD-PVA aggregates were not observed in MultiDots synthesized *via* sonication processes. These findings are consistent with previous reports.[52]

When comparing fluorescence intensity; however, it should be noted that the number of QDs encapsulated likely varies between PVA aggregate and MultiDot samples using the different synthesis methods. CL spectroscopy (Fig. 5(A)–(C)) of the three species was expected to yield similar results to MultiDots produced using EE approaches not incorporating PVA surfactants (Fig. 3(D)–(F)), including a QD bandgap peak at ~1.83 eV, a QD emission peak at ~2.08 eV, and potential CdO defect peaks at ~2.28. For MultiDots isolated from the manual shaking sample, band gap peak (1.83 eV) and oxidation peaks (2.23 eV) were observed (Fig. 5(A)). Corresponding to the low observed fluorescence, an emission peak could not be extracted from curve fit data. For QD-PVA aggregates, the emission peak at 2.01 eV dominated (Fig. 5(B)). MultiDots synthesized *via* sonication exhibited a slightly red-shifted band gap peak (1.80 eV, possibly as a result of PVA presence), a dominant emission peak at 2.01 eV, and a shoulder at ~2.30 eV, suggesting the possible presence of CdO (Fig. 5(C)).

In comparison to the CL spectra for –BCPs synthesized *via* EE, the oxidation peak intensity followed the general order of: manual shaking IS –COOH (PVA aggregates removed) > EE –NH_2 > EE –COOH > EE –OH/sonication IS –COOH with PVA > manual shaking IS PVA aggregates. Thus, composites incorporating PVA yielded the greatest resistance to surface oxidation (and the highest fluorescence) signal compared to composites not incorporating PVA. The impact of PVA molecules on QD oxidation may result from its ability to interact with –COOH groups in the BCP chains (most likely through hydrogen bonding) or simply the large excess of PVA permitting its incorporation into the micelle structure. Unfortunately, PVA does not present readily functionalizable groups needed for bioconjugation nor does it impart colloidal stability to the aggregates (Fig. S7†). Additionally, MultiDots in biological applications would most likely be diluted into aqueous media serving as a PVA concentration sink. In this case, adsorbed PVA would equilibrate with the surrounding media, reducing its ability to protect against oxidation. Thus, QD passivation using PVA alone is not advised. A further observation from these experi-

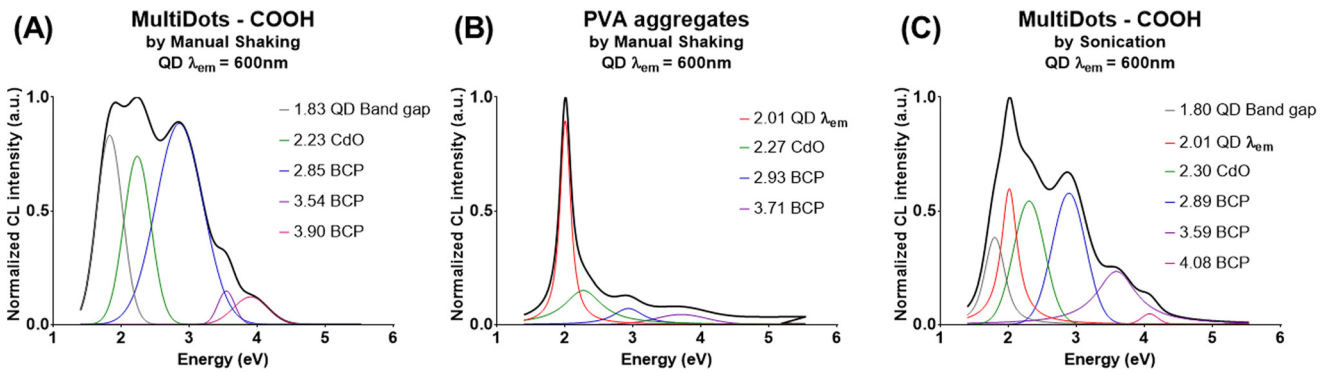

Fig. 5 CL spectroscopy of (A) MultiDots passivated using BCPs terminated with –COOH synthesized *via* manual shaking, (B) QD-PVA aggregates synthesized *via* using manual shaking, and (C) MultiDots passivated using BCPs terminated with –COOH synthesized *via* sonication.

ments is that the speed of composite formation matters. Manual shaking produces large emulsion droplets, increasing the time to micelle formation because of extended solvent evaporation rates. MultiDots formed *via* manual shaking with the same materials at the same concentrations as EE processes, but with slower kinetics exhibited substantially reduced fluorescence intensity and significantly higher defect peaks. Similar observations have been reported for ligand exchange processes; methods that favour rapid coating formation improve fluorescence retention following aqueous phase transfer.[53]

Discussion

These results are consistent with the expectation that BCP micelle formation is strongly kinetically controlled.[54] When large hydrophobic encapsulants, such as QDs, are present, nanocomposite formation depends on the aggregation rates of the encapsulants and BCPs and BCP-encapsulant interactions.[37,55] The EE-SA method is essentially a semi-batch adaptation of the IS method introduced by Hayward,[32] in which interfacial instabilities at a droplet surface generate droplet fission. Combined with solvent evaporation, micelles encapsulating NPs are formed. However, in the EE-SA method, solvent evaporation takes place in ~5 minutes *versus* ~1.5 hours for batch IS. Thus, it is likely that EE-SA micelles are more disordered than those generated in batch. NP encapsulation is enhanced by accumulation of the NPs at the droplet surface (*e.g.*, similar to a Pickering emulsion), and depends most strongly on the hydrophobic block length.[32,56] As the hydrophobic blocks employed in this study were identical, NP-BCP association times were likely unchanged for the three polymers. However, the addition of charged groups to the hydrophilic block terminus would change the BCP–BCP aggregation kinetics, which we infer from differences in observed particle sizes and morphology. Interestingly, –COOH terminated and $-NH_2$ terminated MultiDots were more likely to display QD aggregates, indicating that NP aggregation likely occurred faster than BCP–BCP aggregation and subsequent micelle formation for these compositions.

Once formed, the micelles produced by EE-SA are most likely kinetically frozen. Large BCPs, such as the PS-PEO utilized here, have not been observed to readily undergo BCP chain exchange,[57–59] especially given the high glass transition temperature of the PS block.[60,61] Thus, it is unlikely that chain exchange enables QD oxidation. This is further supported by the observation that QD fluorescence intensity is steady for 7 days. If chain exchange were occurring over the scale of days, fluorescence should continue to decline with oxidation enabled by exposure to the aqueous environment. For the same reason, it is unlikely that fluorescence loss and oxidation results from changes in micelle structure that promote oxygen permeability. The majority of fluorescence loss occurs during or within 24 hours of micelle formation, suggesting that this effect most likely results from changes in aggregation kinetics as opposed to structural changes.

In this context, the role of BCP chain charge repulsion in the final product, when many chains are available to protect QDs, is probably less important than its role in slowing aggregation kinetics. Prior to encapsulation, QDs most likely segregate to the oil droplet-aqueous interface, and are thus exposed to the aqueous phase. During this time, the organic QDs are protected by only a limited number of short ligands. Loss of QD fluorescence most likely results from oxidation of the QD surface through ligand loss during composite synthesis. The aqueous media employed in most polymer coating approaches serves as a sink for QD ligands, which are not covalently bound, but rather adsorbed, to the QD surface. Most QD ligands are L-type Lewis bases, which has been shown to result in metal etching of the QD surface through ligand–metal–carboxylate complex formation.[18] This can lead to fluorescence loss even the presence of an insulating shell because the surface and core wave functions are not separated.[62] This hypothesis is supported by the observation that synthesis under a N_2 blanket did not alter resultant composite QY and that PVA, which can hydrogen bond with ligands to stabilize them, enhanced fluorescence. In this case, our results would likely equally apply to interdigitated polymer coating methods of QD passivation (*e.g.*, Gao *et al.*[7]), provided that the association kinetics are sufficiently slow to allow for ligand desorption.

One approach to address this issue would be to increase the thickness of the ZnS shell. However, this is impractical for many applications, as shell thickness ~20 nm or greater may be required. Also, most commercial QDs have shell thicknesses of only ~1–3 nm. An alternative would be to utilize BCPs with mixed functional groups (*i.e.*, –OH and either –COOH, or $-NH_2$), such as zwitterionic materials currently being investigated.[30] However, it should be noted that only a fraction of terminal groups will likely reside on the micelle surface,[51] especially if large BCPs are used. Also, the solubility tuning approach might be employed, in which NP solubility is closely match to the BCP hydrophobic block to promote rapid assembly and precise localization within the micelle structure.[37,63] Alternatively, processes with faster aggregation kinetics, such as nanoprecipitation, may be preferred. These approaches reduce QD exposure time to the aqueous environment, where oxidation likely originates. Although the exact mechanism of oxidative degradation observed here is not clear, it is likely similar to that reported by van Sark *et al.*,[24,25] in which oxygen radicals present in water diffuse to the grain boundary of the ZnS shell to form CdO and the QD surface. Additionally, PVA surfactant provided a strong protective effect against oxidation. It is unclear what role PVA plays in the oxidation process, whether it presents a higher diffusive barrier to oxygen molecules, serves as a sink for reactive oxygen radicals, or simply has better affinity with unprotected regions of the QD surface, and this should be further investigated. These results highlight an often overlooked aspect of polymer NP and nanocomposite synthesis, which is the role of surfactant in the final product. Nonionic surfactants, such as PVA, are often considered benign, but these results clearly indicate that PVA

may be a critical element in preserving QD functionality. Nonetheless, PVA-QD aggregates formed from PVA alone are not colloidally stable, nor do they present readily functionalizable groups, limiting their suitability as applied functional materials. Similarly, BCPs terminated with –OH showed the lowest oxidation, but the lack of bioconjugation chemistries that can be performed on this functional group make it an unsuitable choice for many applications. However, other polymers may yield similar protection against oxidation, while offering biocompatible features and should be considered.[64,65] Further, the use of sacrificial oxidation layers that has been adopted for many organic QDs may improve performance.[66–68]

Conclusions

Enabled by surfactant-free EE-SA and integrated CL/XPS, interactions between amphiphilic BCPs and the QD surface were investigated for the first time. Specifically, an oxidative degradation pathway tied to CdO formation during aqueous phase transfer was identified *via* CL and XPS measurements. However, we acknowledge the need for more comprehensive analysis of oxidized QDs to precisely characterize the emergence of CdO, SeO_2, and/or $CdSeO_3$,[69] some of which were below the limit of detection in this study. CdO formation was more pronounced for composites formed from charged BCPs or those that formed with slower self-assembly kinetics, corresponding to observed declines in fluorescence intensity. These data suggest that BCPs should be chosen to increase aggregation kinetics, while preserving functionalizable groups. Further, EE-SA and other high throughput synthesis processes with rapid kinetics[55,70] should be employed. Additionally, the use of surfactants should be considered. These data suggest that the protective effect of PVA is maximized if present during synthesis; thus, addition post-synthesis is unlikely to provide strong benefit. These data provide important insight into oxidation processes occurring during QD aqueous phase transfer and provide critical guidance toward materials and synthesis selection that will enhance biological translation capacity of QDs.

Experimental

Materials

Poly(styrene-*b*-ethylene oxide) BCPs (PS 9.5 kDa : PEO 18.0 kDa) with (–OH, –COOH, and $–NH_2$) terminal groups were purchased from Polymer Source Inc. (Montreal, Canada). Powdered, hydrophobic CdSe/ZnS QDs (λ_{em} = 550 nm or 600 nm) were purchased from Ocean NanoTech (San Diego, CA). Hamilton™ metal hub blunt point needles (27 gauge, 410 μm o.d.; 210 μm i.d.) and glass luer lock syringes (1 mL) were purchased from ThermoFisher Scientific. Polytetrafluoroethylene (PTFE) heat shrink tubing (30 gauge, 0.006″ wall, shrink ratio 2 : 1) was purchased from Component Supply company (Lakeland, FL). MilliporeSigma Milli-QTM ultrapure water system was used to prepare Milli-Q ultrapure water. HPLC grade (99.8%) chloroform was purchased from Sigma-Aldrich.

QD encapsulation in BCP micelles *via* EE-SA

Most electrospray techniques atomize a conductive liquid into air, necessitating surfactants such as polyvinyl alcohol (PVA) to reduce the surface tension for deforming the liquid interface when organic solutions are used as the driving fluid. Here, we employed electrohydrodynamic emulsification (EE) to generate solutions for self-assembly (SA) or BCP micelles encapsulating QDs. In EE, the conductivity of the fluids is reversed, *i.e.* a dielectric fluid such as the polymer/organic solution is dispersed into a more conductive fluid, *i.e.*, distilled water (Fig. S8†).[39] The electric potential between the needle and the grounding electrode induces the motion of charge carriers in the conductive fluid (*i.e.*, electrohydrodynamic flow) that generates a fine emulsion of ≤10–100 μm droplets[71] without the need for surfactant. In the EE apparatus, a PTFE heat shrink tubing insulated, 27 gauge, stainless steel needle connected to a 1 mL glass syringe with a luer lock was used to deliver the organic phase. A stainless steel grounding wire encased in PTFE heat shrink tubing and with 1 cm of its end exposed was positioned 1 cm away from the tip of the needle inside a 15 mL glass vial containing 10 mL of Milli-Q water. The organic phase was delivered at 12.7 mL h^{-1} under an applied voltage of −2500 V.

To form MultiDots, powdered QDs were dissolved and stored in toluene (3.5 mg mL^{-1}). To reconstitute QDs into chloroform (1.75 mg mL^{-1}), solvent exchange was performed using methanol/acetone (2 : 3 v/v). The organic phase for EE-SA consisted of 100 μL of PS-PEO (10 mg mL^{-1} in chloroform) and 100 μL of QDs (1.75 mg mL^{-1} in chloroform). Emulsifying the organic phase *via* EE generated a milky solution of emulsion droplets in Milli-Q water. After emulsification, the solution was transferred into a glass Petri dish (diameter: 10 cm) on a rocker in a fume hood to promote solvent evaporation. Under ambient condition, the cloudy emulsion became transparent after ∼5 to 10 minutes. The solution was left on a rocker for total 2 hours. QD encapsulation in BCP micelles *via* IS: MultiDots encapsulating QDs *via* the interfacial instability (IS) process were formed as described in Sun *et al.*[52] Briefly, the organic phase (red QDs, 100 μL of stock solution of 1.75 mg mL^{-1} in chloroform, and PS-PEO-COOH, 100 μL of stock solution of 10 mg mL^{-1} in chloroform) was added to aqueous PVA (5 mg mL^{-1}, MW = 13k–23k, 87–89% hydrolyzed) and mixed *via* manual shaking. The emulsion droplet solution formed was in the fume hood to evaporate the organic solvent. After 2.5 hours, QD-PVA aggregates were observed at the bottom of the collection vial. These aggregates were separated from MultiDots dispersed in PVA solution by centrifugation, followed by supernatant removal by pipetting. In addition, MultiDots were synthesized using the same procedure, but replacing manual shaking mixing methods with probe sonication. QD-PVA aggregates were not observed in sonication solution.

Nanocomposite characterization

MultiDot nanocomposites sizes were determined from TEM images as described previously[39] using an FEI Tecnai G2 Bio Twin TEM at 80 kV with negative staining. Analysis was performed using NIH Image J to determine the Feret length, the longest dimension of the particle. QD absorbance was determined using a Genesys 6 UV-Visible spectrophotometer. QD encapsulation efficiency was determined by comparing UV-Visible spectroscopy measurements at 488 nm for MultiDots before and after recovery. Fluorescence and QY were measured using a PTI Quantamaster fluorometer with Rhodamine 6G in ethanol as a reference dye as described previously.[72]

Photoluminescence

MultiDots were evaluated for photoluminescence using a Photon Technology International PTI-810 fluorometer (excitation: 360 nm, lamp power: 75 W, detector voltage: 1100 V). MultiDots were evaluated at the concentration at which they were synthesized using 80 μL of sample in a quartz cuvette. To evaluate fluorescence stability, fluorescence intensity was measured in triplicate samples daily over 7 days. MultiDots were stored at room temperature in the dark.

Cathodoluminescence spectroscopy (CL)

Samples were dried on a stainless-steel sheet. Cathodoluminescence experiments were performed using a Physical Electronics Inc. (PHI) 110-10 glancing incidence electron gun operated at an electron beam voltage of 1.0 kV and an emission current of 1.0 μA under ultrahigh vacuum conditions. The emitted photons were collected by a CaF_2 lens in vacuum, and passed through a sapphire viewport into an Oriel Fnumber matcher. An Oriel monochromator was utilized to disperse the light with a grating with a 300 nm blaze onto an Andor iDus open-electrode charge-coupled detector.

X-ray photoelectron spectroscopy (XPS)

Samples were dried on a stainless steel sheet. XPS was performed using a PHI Versaprobe 5000 XPS system with a monochromatic Al K-α X-ray source with X-ray energies of 1486.6 eV. X-rays were produced by an incident electron beam on an Al anode. Then, these X-rays were passed through a quartz crystal monochromator followed by an Al window to ensure only Al K-α X-rays reach the sample. Photoelectrons emitted from samples were collected in a hemispherical analyzer (HSA) and detected by channel plates. The HSA has an energy resolution of 0.046 eV as calibrated by the Fermi edge of the valence band of Au.

Zeta potential measurements

The surface charge of micelles synthesized from BCPs terminated with –OH, –COOH, or $–NH_2$ was measured using a ZetaPALS potential analyzer (Brookhaven Instruments corporation) in five serial measurements.

Author contributions

The authors are using the CRediT attribution scheme. Conceptualization – JOW, LJB; data curation – KHL, BAN, CM, LJB, JOW; formal analysis – KHL, BAN, CM, LJB, JOW; funding acquisition – LB, JOW; investigation – KHL, BAN, CM; methodology – KHL, BAN, CM, LJB, JOW; project administration – JOW, resources – LJB, JOW; software – KHL, BAN, CM, LJB, JOW; supervision – LJB, JOW; validation – KHL, BAN, CM, LJB, JOW; visualization – KHL, BAN, CM; writing – original draft – KHL, BAN, CM; writing – review & editing KHL, BAN, CM, LJB, JOW.

Conflicts of interest

Jessica O. Winter is a founder and maintains equity interest in Core Quantum Technologies (CQT), a company developing QD reagents for cancer diagnostics. CQT provided no support or materials for this work.

Acknowledgements

This work was funded by the National Science Foundation under grants CMMI-1344567, DMR-1420451, and DMR-2011876.

Notes and references

1 C. J. Murphy, *Peer reviewed: optical sensing with quantum dots*, ACS Publications, 2002.
2 W. J. Parak, D. Gerion, T. Pellegrino, D. Zanchet, C. Micheel, S. C. Williams, R. Boudreau, M. A. Le Gros, C. A. Larabell and A. P. Alivisatos, *Nanotechnology*, 2003, **14**, R15.
3 P. Alivisatos, *Nat. Biotechnol.*, 2004, **22**, 47.
4 C. M. Niemeyer, *Angew. Chem., Int. Ed.*, 2001, **40**, 4128–4158.
5 W. C. Chan and S. Nie, *Science*, 1998, **281**, 2016–2018.
6 M. Bruchez Jr., M. Moronne, P. Gin, S. Weiss and A. P. Alivisatos, *Science*, 1998, **281**, 2013–2016.
7 X. H. Gao, Y. Y. Cui, R. M. Levenson, L. W. K. Chung and S. M. Nie, *Nat. Biotechnol.*, 2004, **22**, 969–976.
8 I. L. Medintz, H. T. Uyeda, E. R. Goldman and H. Mattoussi, *Nat. Mater.*, 2005, **4**, 435–446.
9 A. V. Isarov and J. Chrysochoos, *Langmuir*, 1997, **13**, 3142–3149.
10 R. E. Galian and J. C. Scaiano, *Photochem. Photobiol. Sci.*, 2009, **8**, 70–74.
11 Y. Chen and Z. Rosenzweig, *Anal. Chem.*, 2002, **74**, 5132–5138.
12 H. Li and X. Wang, *Sens. Actuators, B*, 2008, **134**, 238–244.
13 X. Hu, P. Zrazhevskiy and X. Gao, *Ann. Biomed. Eng.*, 2009, **37**, 1960–1966.
14 K. M. Gattás-Asfura and R. M. Leblanc, *Chem. Commun.*, 2003, 2684–2685.

15 M. Jones, J. Nedeljkovic, R. J. Ellingson, A. J. Nozik and G. Rumbles, *J. Phys. Chem. B*, 2003, **107**, 11346–11352.
16 Y. Zhang, P. Jing, Q. Zeng, Y. Sun, H. Su, Y. A. Wang, X. Kong, J. Zhao and H. Zhang, *J. Phys. Chem. C*, 2009, **113**, 1886–1890.
17 J.-L. Chen and C.-Q. Zhu, *Anal. Chim. Acta*, 2005, **546**, 147–153.
18 N. C. Anderson, M. P. Hendricks, J. J. Choi and J. S. Owen, *J. Am. Chem. Soc.*, 2013, **135**, 18536–18548.
19 E. Kalwarczyk, N. Ziebacz, T. Kalwarczyk, R. Holyst and M. Fialkowski, *Nanoscale*, 2013, **5**, 9908–9916.
20 A. M. Smith, H. Duan, M. N. Rhyner, G. Ruan and S. Nie, *Phys. Chem. Chem. Phys.*, 2006, **8**, 3895–3903.
21 L. M. Qi, H. Colfen and M. Antonietti, *Nano Lett.*, 2001, **1**, 61–65.
22 J. Aldana, Y. A. Wang and X. Peng, *J. Am. Chem. Soc.*, 2001, **123**, 8844–8850.
23 J. Aldana, N. Lavelle, Y. Wang and X. Peng, *J. Am. Chem. Soc.*, 2005, **127**, 2496–2504.
24 W. G. J. H. M. van Sark, P. L. T. M. Frederix, D. J. Van den Heuvel, H. C. Gerritsen, A. A. Bol, J. N. J. van Lingen, C. de Mello Donegá, and A. Meijerink, *J. Phys. Chem. B*, 2001, **105**(35), 8281–8284.
25 W. G. J. H. M. van Sark, P. L. T. M. Frederix, A. A. Bol, H. C. Gerritsen and A. Meijerink, *ChemPhysChem*, 2002, **3**, 871–879.
26 M. Gao, S. Kirstein, H. Möhwald, A. L. Rogach, A. Kornowski, A. Eychmüller and H. Weller, *J. Phys. Chem. B*, 1998, **102**, 8360–8363.
27 N. Erathodiyil and J. Y. Ying, *Acc. Chem. Res.*, 2011, **44**, 925–935.
28 B. Dubertret, P. Skourides, D. J. Norris, V. Noireaux, A. H. Brivanlou and A. Libchaber, *Science*, 2002, **298**, 1759–1762.
29 G. Ruan and J. O. Winter, *Nano Lett.*, 2011, **11**, 941–945.
30 N. Zhan, G. Palui, M. Safi, X. Ji and H. Mattoussi, *J. Am. Chem. Soc.*, 2013, **135**, 13786–13795.
31 G. Ruan, G. Vieira, T. Henighan, A. R. Chen, D. Thakur, R. Sooryakumar and J. O. Winter, *Nano Lett.*, 2010, **10**, 2220–2224.
32 J. Bae, J. Lawrence, C. Miesch, A. Ribbe, W. Li, T. Emrick, J. Zhu and R. C. Hayward, *Adv. Mater.*, 2012, **24**, 2735–2741.
33 Z. Ning, O. Voznyy, J. Pan, S. Hoogland, V. Adinolfi, J. Xu, M. Li, A. R. Kirmani, J.-P. Sun, J. Minor, K. W. Kemp, H. Dong, L. Rollny, A. Labelle, G. Carey, B. Sutherland, I. G. Hill, A. Amassian, H. Liu, J. Tang, O. M. Bakr and E. H. Sargent, *Nat. Mater.*, 2014, **13**, 822–828.
34 G. T. Hermanson, *Bioconjugate techniques*, Academic press, 2013.
35 M. S. Souva, G. M. Nabar, J. O. Winter and B. E. Wyslouzil, *J. Colloid Interface Sci.*, 2018, **512**, 411–418.
36 J.-H. Park, G. von Maltzahn, E. Ruoslahti, S. N. Bhatia and M. J. Sailor, *Angew. Chem.*, 2008, **120**, 7394–7398.
37 G. M. Nabar, J. O. Winter and B. E. Wyslouzil, *Soft Matter*, 2018, **14**, 3324–3335.
38 A. D. Duong, G. Ruan, K. Mahajan, J. O. Winter and B. E. Wyslouzil, *Langmuir*, 2014, **30**, 3939–3948.
39 K. H. Lee, M. Ireland, B. L. Miller, B. E. Wyslouzil and J. O. Winter, *J. Colloid Interface Sci.*, 2021, **586**, 445–456.
40 J. Xu, Q. Fan, K. D. Mahajan, G. Ruan, A. Herrington, K. F. Tehrani, P. Kner and J. O. Winter, *Nanotechnology*, 2014, **25**, 195601.
41 S. Ninomiya and S. Adachi, *J. Appl. Phys.*, 1995, **78**, 4681–4689.
42 M. A. Hegazy and A. M. A. El-Hameed, *NRIAG J. Astron. Geophys.*, 2014, **3**, 82–87.
43 U. Lunz, J. Kuhn, F. Goschenhofer, U. Schüssler, S. Einfeldt, C. R. Becker and G. Landwehr, *J. Appl. Phys.*, 1996, **80**, 6861–6863.
44 P. Phukan and D. Saikia, *Int. J. Photoenergy*, 2013, **2013**, 728280.
45 S. B. Aziz, S. Hussein, A. M. Hussein and S. R. Saeed, *Int. J. Met.*, 2013, **2013**, 123657.
46 V. P. Savchyn, A. I. Popov, O. I. Aksimentyeva, H. Klym, Y. Y. Horbenko, V. Serga, A. Moskina and I. Karbovnyk, *Low Temp. Phys.*, 2016, **42**, 597–600.
47 F. P. Koffyberg, *Phys. Rev. B: Solid State*, 1976, **13**, 4470–4476.
48 J. J. Yeh and I. Lindau, *At. Data Nucl. Data Tables*, 1985, **32**, 1–155.
49 M. P. Seah and W. A. Dench, *Surf. Interface Anal.*, 1979, **1**, 2–11.
50 J. F. Moulder and J. Chastain, *Handbook of X-ray Photoelectron Spectroscopy: A Reference Book of Standard Spectra for Identification and Interpretation of XPS Data*, Physical Electronics Division, Perkin-Elmer Corporation, Eden Prairie, MN, 1992.
51 J. T. Koberstein, *J. Polym. Sci., Part B: Polym. Phys.*, 2004, **42**, 2942–2956.
52 Y. Sun, L. Mei, N. Han, X. Ding, C. Yu, W. Yang and G. Ruan, *Nanoscale Res. Lett.*, 2017, **12**, 434.
53 R. A. Sperling and W. J. Parak, *Philos. Trans. R. Soc., A*, 2010, **368**, 1333–1383.
54 H. Cui, Z. Chen, S. Zhong, K. L. Wooley and D. J. Pochan, *Science*, 2007, **317**, 647–650.
55 B. K. Johnson and R. K. Prud'homme, *Aust. J. Chem.*, 2003, **56**, 1021–1024.
56 K. Hpone Myint, J. R. Brown, A. R. Shim, B. E. Wyslouzil and L. M. Hall, *J. Phys. Chem. B*, 2016, **120**(44), 11582–11594.
57 B. K. Johnson and R. K. Prud'homme, *Phys. Rev. Lett.*, 2003, **91**, 118302.
58 T. Nicolai, O. Colombani and C. Chassenieux, *Soft Matter*, 2010, **6**, 3111–3118.
59 R. Lund, L. Willner, D. Richter and E. E. Dormidontova, *Macromolecules*, 2006, **39**, 4566–4575.
60 Y. Wang, R. Balaji, R. P. Quirk and W. L. Mattice, *Polym. Bull.*, 1992, **28**, 333–338.
61 Y. Wang, C. M. Kausch, M. Chun, R. P. Quirk and W. L. Mattice, *Macromolecules*, 1995, **28**, 904–911.

62 Y. Chen, J. Vela, H. Htoon, J. L. Casson, D. J. Werder, D. A. Bussian, V. I. Klimov and J. A. Hollingsworth, *J. Am. Chem. Soc.*, 2008, **130**, 5026–5027.
63 J. Wang, W. Li and J. Zhu, *Polymer*, 2014, **55**, 1079–1096.
64 R. Calzada, C. M. Thompson, D. E. Westmoreland, K. Edme and E. A. Weiss, *Chem. Mater.*, 2016, **28**, 6716–6723.
65 J. Ko, B. G. Jeong, J. H. Chang, J. F. Joung, S. Y. Yoon, D. C. Lee, S. Park, J. Huh, H. Yang, W. K. Bae, S. G. Jang and J. Bang, *NPG Asia Mater.*, 2020, **12**, 19.
66 Z. C. Li, W. Yao, L. Kong, Y. X. Zhao and L. Li, *J. Am. Chem. Soc.*, 2015, **137**, 12430–12433.
67 L. Huang, Z. C. Li, C. Y. Zhang, L. Kong, B. Wang, S. Q. Huang, V. Sharma, H. Y. Ma, Q. C. Yuan, Y. Liu, G. Q. Shen, K. F. Wu and L. Li, *Chem. Sci.*, 2019, **10**, 6683–6688.
68 Q. Wan, Z. C. Li, C. Y. Zhang, W. L. Zheng, L. Huang, M. M. Liu, Q. G. Zhang, B. Wang, W. Liu, L. Kong and L. Li, *J. Phys. Chem. C*, 2020, **124**, 28424–28430.
69 J. E. B. Katari, V. L. Colvin and A. P. Alivisatos, *J. Phys. Chem.*, 1994, **98**, 4109–4117.
70 K. H. Lee, G. Yang, B. E. Wyslouzil and J. O. Winter, *ACS Appl. Polym. Mater.*, 2019, **1**, 691–700.
71 M. Sato, T. Hatori and M. Saito, *IEEE Trans. Ind. Appl.*, 1997, **33**, 1527–1534.
72 K. H. Lee, T. Porter and J. O. Winter, *MRS Commun.*, 2019, **9**, 702–709.